Coulomb Collisions in the Solar Wind

Hao Ran

April 2024

Contents

1 Introduction

1.1 Coulomb Collisions

Coulomb collisions play a critical role in shaping the velocity distribution functions of the ions in the solar wind (*Marsch et al. 1983* [13]). They refer to slight deflections of the charged particles due to the interaction among them. Collisions among particles provide the fundamental mechanism through which an ionized plasma increases its entropy and ultimately comes into thermal equilibrium. The occurring rate of Coulomb collisions is relatively low in the solar wind due to its low-density condition, but it is not negligible. In the corona, by contrast, the plasma is much denser, and the collisional processes contribute significantly to the heating and acceleration of the solar wind (*Verscharen et al. 2019* [25]). Table 1 (adopted from *Marsch et al. 2006* [14]) shows the varying Coulomb conditions.

Parameter	Chromosphere	Corona	Solar Wind
n (cm^{-3})	10^{10}	10^7	10
T (K)	10^3	$1 \sim 2 \times 10^6$	10^5
λ_c (km)	1	10^3	10^7

Table 1: Varying Coulomb collisions. Adopted from *Marsch et al. (2006)* [14].

Given the rare collisions, exospheric models, in which the corona evaporates from an assumed exosphere, have been proposed to explain the expansion of the corona (e.g., *Jockers 1970*, *Lemaire and Scherer 1971* [8, 12]). In these models, collisions and waves are neglected, only free protons and electrons move in the gravitational field and interplanetary electric field while being guided by the magnetic field. These models, though are out of fashion today, are still useful for understanding some features of the planetary solar wind. For example, the preferential heating of minor ions in a coronal exosphere can lead to the preferential acceleration of these ions (*Pierrard et al. 2004* [20]).

There are three important concepts that are closely related to Coulomb collisions: **collisional timescale**, **Coulomb number**, and **collisional age**. **Collisional timescale** means the time required for collisions to significantly reduce a non-equilibrium feature (including temperature anisotropies, beams, drifts between two ion species, anisothermal behaviors) in the solar wind. Each non-equilibrium feature has its own collisional timescale, which is determined by the conditions of the plasma. To see the exact expressions for the collisional timescales, one can refer to *Spitzer (1956)* [24], *Schunk (1975)* [23], *Hernandez and Marsch (1985)* [7], and *Wilson et al. (2018)* [26]. The parameters commonly used to describe the collisionality are the "**collisional age**" (A_c, *Kasper et al. 2008* [9]) and the "**Coulomb number**" (N_c, *Kasper et al. 2017* [11]). We will introduce the meaning and derivation of these two properties in Section 2.

1.2 Instabilities in the Solar Wind

Instabilities refer to the mechanisms that transfer energy from free-energy sources, such as distorted particle distributions and large-amplitude waves, to plasma normal modes.

To start with, we introduce wave-particle instabilities, which are driven by departures from Maxwellian equilibrium state of the particle distribution functions. A non-Maxwellian distribution must meet certain conditions for an instability to occur and transferring energy from particles to magnetic and electric fields. This leads to exponential growth of a mode and brings the system closer
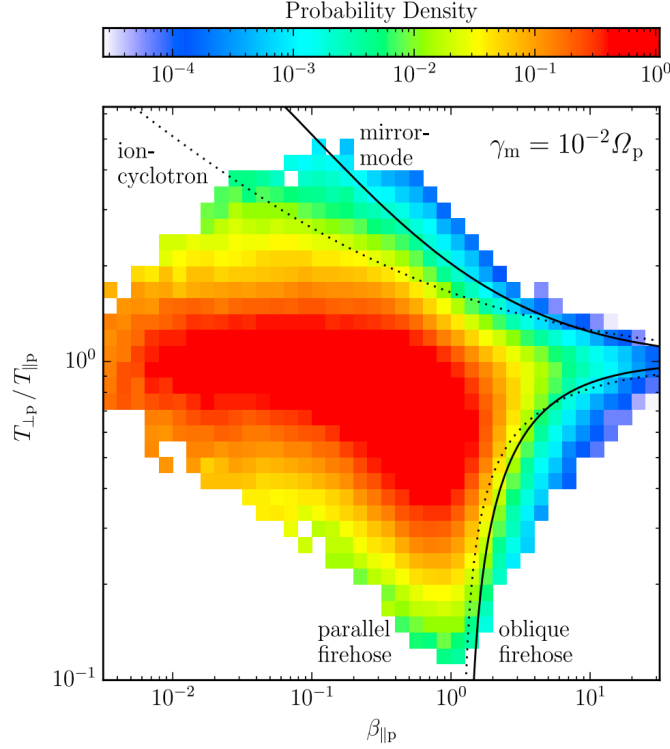
Figure 1: Probability of the pristine solar wind in the $\beta_{\|p} - T_{\perp p}/T_{\|p}$ plane. The instability thresholds for the four instabilities associated with proton temperature are indicated by the lines and the dotted lines. Picture adopted from *Verscharen et al. (2019)* [25].

to local thermodynamic equilibrium. Once the conditions are not met, the system marches towards a state of marginal stability (e.g., *Matteini et al. 2006*, [18]). Temperature anisotropy serves as an indicator of the wave-particle instabilities. As temperature anisotropy departs from unity, anisotropy instabilities such as mirror, ion-cyclotron, parallel, and oblique firehose instabilities arise and act to isotropize the plasma(*Gary 1993, Maruca et al. 2011* [4, 15]). Table 2 lists the instabilities driven by ion temperature instabilities. Figure 1 shows an example of the constraints of all the instabilities in the $\beta_{\|p} - T_{\perp p}/T_{\|p}$ plane. An instability is triggered when the distribution extends beyond the instability threshold. As can be seen, ion-cyclotron instability sets a stricter limit on the departure from isotropy than mirror-mode instability. The constraints from oblique and parallel firehose instabilities are similar, but the latter is slighly more restrictive. Note that anisotropy from other plasma components, such as electrons and alpha particles, can also lead to resonant instabilities. Another energy source of wave-particle instabilities is the relative drift between different plasma components. The velocity difference between the two components can contribute to excess parallel pressure or induce currents, the drifting distributions themselves may resonate with unstable waves as well.

Wave-wave instabilities, unlike wave-particle instabilities, depend sensitively on the amplitudes of plasma fluctuations. The parametric-decay instability (PDI) is a classic example of wave-wave instabilities (*Galeev and Oraevskii 1963*, *Sagdeev and Galeev 1969* [3, 22]). In the low-β_p limit, the PDI causes a finite-amplitude forawrd-propagating Alfvén wave, decaying into a backward-propagating Alfvén wave and a forward-propagating acoustic wave. The dynamics of such instabilities is of importance for the evolution of the solar wind. The compressive acoustic mode can efficiently dissipate and thus heat the plasma (*Barnes 1966* [1]). On the other hand, the backward-propagating

Name	Driven by	Type	Frequency	Maximum growth rate	
				ka_i	$k_\perp$
Fire hose	$T_{\perp i} < T_{\parallel i}$	electromagnetic	magnetosonic whistler	< 1	0
Mirror	$T_{\perp i} > T_{\parallel i}$	predominantly electrostatic	$\omega = 0$	< 1	$> k_\parallel$
Ion cyclotron	$T_{\perp i} > T_{\parallel i}$	electromagnetic	$\omega \lesssim \Omega_i$	$\lesssim 1$	0
Harris	$T_{\perp i} < T_{\parallel i}$	electrostatic+electromagnetic	$\omega < \Omega_i$	< 1	$\sim k_\parallel$

Table 2: Four instabilities driven by ion temperature anisotropies. Table adopted from *Gary et al. (1976)* [5].

Alfvén wave can drive turbulent cascade (*Chandran 2018* [2]).

Finally, Parker Solar Probe (PSP) and Solar Orbiter (SO) represent the latest generation of spacecrafts that are designed to study the solar wind and the Sun. A combined analysis of the data from these two spacecrafts can provide a comprehensive view of the radial evolution of the solar wind, and the role of Coulomb collisions in the expanding plasma. We can address the following questions with PSP and SO observations:

1. How do Coulomb collisions affect the non-equilibrium features (including temperature anisotropies, beams, drifts between different ion species, anisothermal behaviors, etc) in the solar wind as a function of the distance from the Sun?

2. What is difference between Coulomb collisions in the slow solar wind and the fast solar wind?

2 Data and Methods

We obtain ion parameters from SWEAP level 3 data product, and magnetic field parameters from FIELDS level 2 data product. The plasma density is represented by the electron density we get from FIELDS level 3 Quasi-thermal noise (QTN) data product.

2.1 How to calculate Collisional Age and Coulomb number?

The majority of the heating and acceleration of the particles in the solar wind occurs within and around the solar corona. Beyond that region, the bulk speed of the solar wind remains nearly constant and radial. Thus, the time required for a parcel of plasma to travel to a distance r is approximately the expansion time:

$$\tau = r/U_r.$$

The Coulomb number of the parcel of plasma is then defined as:

$$N_c \equiv \frac{\tau}{\tau_c} = \frac{r}{U_r \tau_c},$$

where τ_c is a collisional timescale. The Coulomb number approximates the number of such collisional timescales that elapsed during its journey to the observer. In collisionally old ($N_c \gg 1$) plasma, collisional equilibration has proceeded much farther than in collisionally young ($N_c \ll 1$) plasma. However, the use of Coulomb number to quantify collisions has two obvious limitations. First, the above definition for N_c only allows for a single collision timescale τ_c. Although the correct formula for τ_c can be chosen based on the specific non-equilibrium feature being examined, it is challenging to account for interactions involving multiple deviations from equilibrium. Second, the expression for N_c assumes that τ_c remains constant with distance r from the Sun. In reality, τ_c varies with density and temperature, both of which exhibit significant radial trends. To address the above issues, various studies (*Hernandez et al. 1987, Kasper et al. 2017, Kasper and Klein 2019*) [6, 11, 10] employ an integrated Coulomb number of the form:

$$A_c \equiv \int \frac{dt}{\tau_c} = \int \frac{dr}{U_r(r)\tau_c(r)}.$$

The formulation directly accounts for the radial dependencies of densities, velocities, and temperatures. Note that in Parker Solar Probe's observation region, there is no significant difference between the Coulomb number and the Collisional age. In *Kasper et al. (2017)* [11], the authors approximately equated the two quantities in their paper (e.g., $A_c \equiv \int \nu_c dt \simeq N_c$).

Here, we introduce a brief calculation method for these two physical properties. For more details, please refer to previous works (e.g., *Hernandez et al. 1987, Kasper et al. 2008, 2017, Maruca et al. 2013, Mostafavi et al. 2024* [7, 9, 11, 16, 19]). According to *Maruca (2012)* [17], it is sufficient to consider the "self-collision time" of an ion species j (*Spitzer, 1956* [24]):

$$\tau_j = (14.4s)(\frac{1}{In\Lambda_j})(\frac{m_j}{m_p})^{1/2}(\frac{q_j}{q_p})^{-4}(\frac{n_j}{1cm^{-3}})^{-1}(\frac{T_j}{1K})^{3/2},$$

where

$$\Lambda_j = (\frac{12\pi}{q_p q_j^2})(\frac{\epsilon_0^3 k_B^3 T_j^3}{n_j})^{1/2},$$

is the plasma parameter. Since the ion population of the solar wind is dominated by protons, it is reasonable to define the collisional age of a parcel of plasma to be:

$$A_c = \frac{D}{\tau_p v_p},$$

where D is the distance of the observer to the Sun, v_p is the speed of the solar wind.

The calculation of the Coulomb number here comes from *Hernandez et al. (1987)* [7]:

$$N_c = D/(v_p \tau_c),$$

where

$$\tau_c = 133 \frac{(\omega_{\alpha p})^3}{n_p}, \omega_{\alpha p} = (\frac{2T_\alpha}{m_\alpha} + \frac{2T_p}{m_p})^{1/2}.$$

2.2 How to calculate the temperature anisotropy of an ion species j with PSP data?

The SWEAP level 3 data product offers 6 components of the temperature tensor in the instrument frame, the keywords are "T_TENSOR_INST_x" (x ranges from 0 to 5). The temperature tensor can be represented as:

$$T_{Tensor,Inst} = \begin{bmatrix} T_{xx} & T_{xy} & T_{xz} \\ T_{yx} & T_{yy} & T_{yz} \\ T_{zx} & T_{zy} & T_{zz} \end{bmatrix},$$

where T_{xx} = "T_TENSOR_INST_0", T_{yy} = "T_TENSOR_INST_1", T_{zz} = "T_TENSOR_INST_2", $T_{xy} = T_{yx}$ = "T_TENSOR_INST_3", $T_{xz} = T_{zx}$ = "T_TENSOR_INST_4", $T_{yz} = T_{zy}$ = "T_TENSOR_INST_5". The SWEAP level 3 data product also provides the magnetic field in the instrument frame, the keywords are "B_INST_x" (x ranges from 0 to 2). The magnetic field can then be represented as:

$$B_{Inst} = (B_x, B_y, B_z),$$

where B_x = "B_INST_0", B_y = "B_INST_1", B_z = "B_INST_2". Then, we can calculate $T_\parallel$ as:

$$T_\parallel = B_{Inst} \cdot T_{Tensor,Inst} \cdot B_{Inst}^T / |B_{Inst}|^2.$$

$T_\perp$ can be represented as:
$$T_\perp = 0.5 * (T_{xx} + T_{yy} + T_{zz} - T_\parallel).$$

Finally, we can calculate the temperature anisotropy as $T_\perp/T_\parallel$.

Note that the temperature anisotropy obtained from the above method is usually not accurate enough to meet the requirement of scientific analysis. To obtain a proper temperature anisotropy, we strongly recommend using the bi-Maxwellian distribution to fit the velocity distribution functions (VDF) of the protons. This can be achieved with the following procedure (*Woodham et al. 2021*) [27]:

(1). Transform the measured VDF from instrument coordinate (v_x, v_y, v_z) to field-aligned coordinate $(v_\parallel, v_{\perp 1}, v_{\perp 2})$.

SPAN-A measures the particel velocity in a spherical coordinate: (ϕ, θ, E), where $E = \frac{1}{2}mv^2$ is the kinetic energy of the particle. The spherical coordinates can be transformed into Cartesian coordinates:

$$v_x = v cos\theta cos\phi, \quad v_y = v cos\theta sin\phi, \quad v_z = v sin\theta.$$

Then, we need to transform the distribution from instrument frame (v_x, v_y, v_z) to field-aligned frame ($v_\parallel$, $v_{\perp 1}$, $v_{\perp 2}$). The rotation matrix is:

$$T = \begin{pmatrix} cos\phi & -k_z sin\phi & k_y sin\theta \\ k_z sin\phi & k_y^2 + k_z^2 cos\phi & k_y k_z(1 - cos\phi) \\ -k_y sin\phi & k_y k_z(1 - cos\phi) & k_z^2 + k_y^2 cos\phi \end{pmatrix},$$

where $\hat{k} = \frac{\hat{x} \times \hat{b}}{|\hat{x} \times \hat{b}|}$ is the unit vector along the rotation axis, $\hat{x} = (1, 0, 0)$ is the unit vector pointing towards the Sun, and $\phi = arccos(\frac{\hat{x} \cdot \hat{b}}{|\hat{x} \cdot \hat{b}|})$ represent the angle between $\hat{b}$ and $\hat{x}$.

(2). Use a bi-Maxwellian function to fit 6 parameters (number density n, the bulk velocity ($u_\parallel$, $u_{\perp 1}$, $u_{\perp 2}$) and the thermal velocity ($\omega_\parallel$, $\omega_\perp$)) that determine the VDF of the particle. We use a non-linear least squares fitting method that minimizing

$$\chi = \sum_{i=1}^{N} [\log(f_{model,i}) - \log(f_{meas,i})]^2$$

for N fitting points, where f_{model} is the predicted value and f_{meas} is the measured value. The 3D bi-Maxwellian model is:

$$f(\mathbf{v}) = f(v_\parallel, v_{\perp 1}, v_{\perp 2}) = \frac{n}{\pi^{3/2} \omega_\perp^2 \omega_\parallel} exp - [(\frac{v_\parallel - u_\parallel}{\omega_\parallel})^2 + (\frac{v_{\perp 1} - u_{\perp 1}}{\omega_\perp})^2 + (\frac{v_{\perp 2} - u_{\perp 2}}{\omega_\perp})^2].$$

With the fitted thermal speed $\omega_\parallel$ and $\omega_\perp$, we can calculate the temperature parallel/perpendicular to the magnetic field as: $T_{\parallel,\perp} = \frac{m}{2k_B} \omega_{\parallel,\perp}^2$.

2.3 How to calculate the marginal stability threshold?

The marginal stability threshold can be defined as a contour of constant maximum growth rate γ_m at any $\mathbf{k}$ through parameter space for a given instability. Assuming that only a couple of parameters (e.g., $\beta_{\parallel j}$ and $T_{\perp j}/T_{\parallel j}$) have a significant influence on the growth rate of an instability, we can construct a parametric model for the instability threshold:

$$\frac{T_{\perp j}}{T_{\parallel j}} = 1 + \frac{a}{(\beta_{\parallel j} - c)^b},$$

where a, b, and c are constant parameters calculated from fits to solutions of the hot plasma dispersion relation. The values for a, b, and c are different for four different unstable modes that are driven by proton temperature anisotropies. We show the best-fit values for these paramters in Table 3.

Instability	a	b	c
$\gamma_m = 10^{-2}\Omega_p$			
Ion-cyclotron	0.649	0.400	0.000
Mirror Mode	1.040	0.633	-0.012
Parallel firehose	-0.647	0.583	0.713
Oblique firehose	-1.447	1.000	-0.148
$\gamma_m = 10^{-3}\Omega_p$			
Ion-cyclotron	0.437	0.428	-0.003
Mirror Mode	0.801	0.763	-0.063
Parallel firehose	-0.497	0.566	0.543
Oblique firehose	-1.390	1.005	-0.111
$\gamma_m = 10^{-4}\Omega_p$			
Ion-cyclotron	0.367	0.364	-0.011
Mirror Mode	0.702	0.674	-0.009
Parallel firehose	-0.408	0.529	0.410
Oblique firehose	-1.454	1.023	-0.178

Table 3: Best-fit values for isocontours of constant maximum growth rate at $\gamma_m = 10^{-2}\Omega_p$, $\gamma_m = 10^{-3}\Omega_p$, and $\gamma_m = 10^{-4}\Omega_p$. Table adopted from *Verscharen et al. (2019)* [25].

3 Results

3.1 Instability Analysis of Encounters 9 and 10

We plot the in-situ measurements of PSP at encounter 9 from 20:00 UT on August 8 2021 to 23:50 UT on August 9 2021 in Figure 2. This interval is selected because the velocity distribution functions (VDFs) of both protons and alphas are well observed. In panels (a) and (b), we show the azimuthal fluxes of protons and alphas, respectively. The result shows that most of the VDFs are captured by SPAN. Panel (c) shows the normalized magnetic field magnitude and the radial component. Patchy switchbacks are observed. Panel (d) shows the radial velocity of protons (black), the radial velocity of alphas (red), the differential speed between alphas and protons (blue), and the local Alfvén speed (green). We can see that the $V_{\alpha R}$ is generally larger than V_{pR}, generating a differential speed ($V_{\alpha p} > 0$) between them. The differential speed is well limited by the local Alfvén speed ($V_{\alpha p} < V_A$). Panel (e) shows the number density of protons and alphas. Note that the density here (as well as the temperature data below) are from SPAN moment measurement, and its accuracy is still subject to verification. Panel (f) shows the temperature anisotropy of protons and alphas. The result indicates that both protons and alphas are preferentially heated in the perpendicular direction, with alphas being more anisotropic than protons. Panel (g) shows the temperature (in eV) of protons and alphas. The fact that alphas are faster and hotter than protons indicate that alphas are preferentially heated and accelerated in the solar wind. This might be due to the resonant interaction between the particles and the waves. Panel (h) shows the collisional age of the plasma. Panel (i) shows the radial Alfvén Mach number.

We show the probability distribution of the pristine solar wind in the $\beta_{p\|} - T_{p\perp}/T_{p\|}$ plane using PSP observations of encounters 9 and 10 in Figure 3 (fast solar wind with $V_p \geq 400km/s$) and Figure 4 (slow solar wind with $V_p < 400km/s$). As seen in Figure 3, the fast solar wind is well constrained by three of the four instabilities: mirror mode, parallel firehose, and oblique firehose. A significant
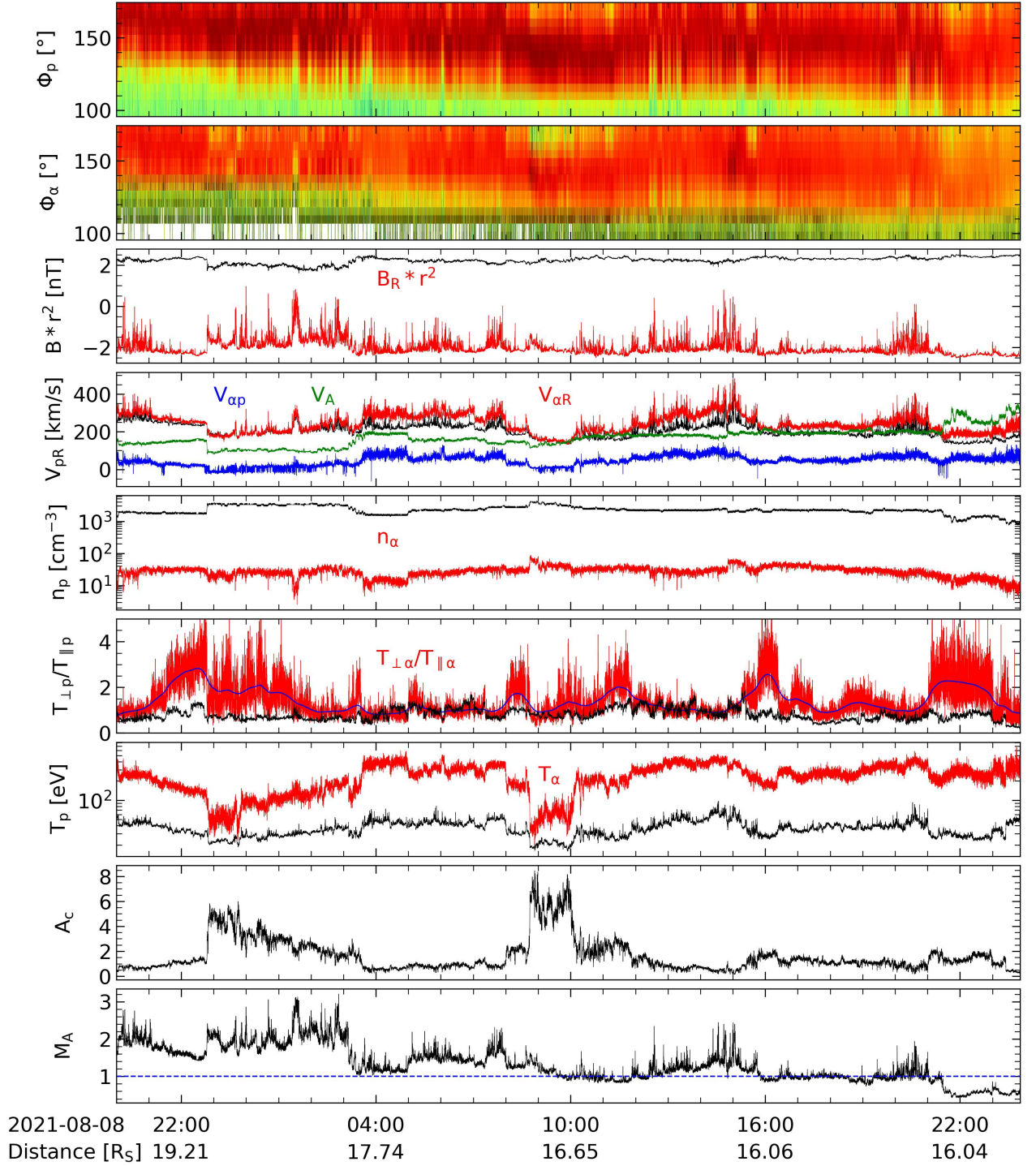
Figure 2: PSP measurements at encounter 9 from 2021-08-08 20:00 to 2021-08-09 23:50. (a) Azimuthal fluxes of protons. (b) Azimuthal fluxes of alphas. (c) Normalized (to 1 AU values) magnetic field magnitude and radial component (red). (d) Radial velocity of protons, radial velocity of alphas (red), differential speed between alphas and protons (blue), local Alfvén speed (green). (e) Number density of protons and alphas (red). (f) Temperature anisotropy of protons and alphas (red). (g) Temperature (in eV) of protons and alphas (red). (h) Collisional Age. (i) Radial Alfvén Mach number.
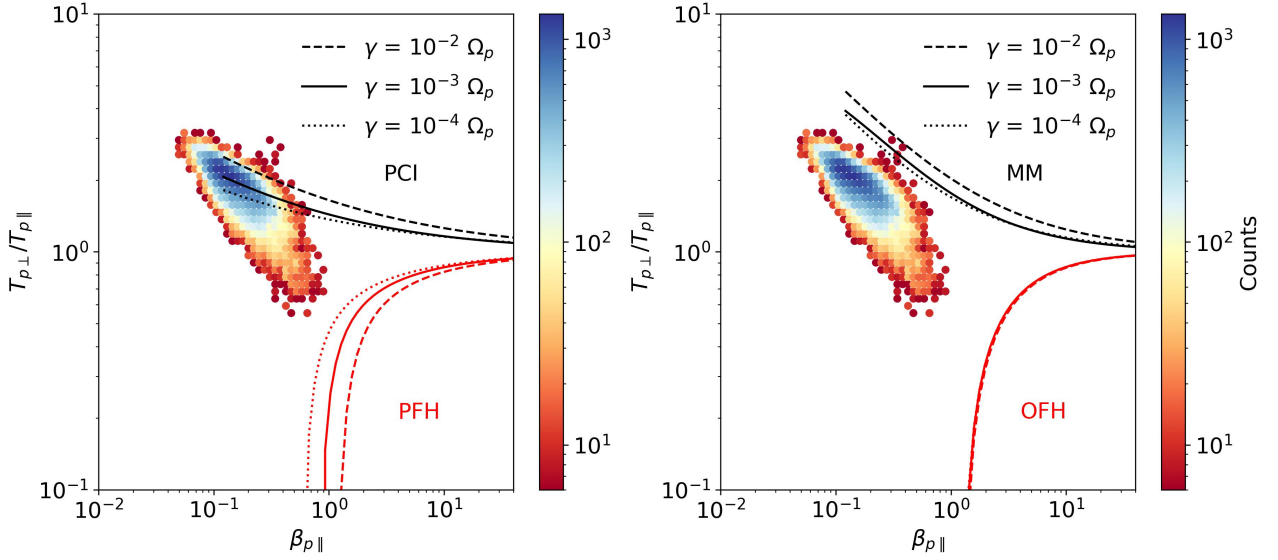
Figure 3: Probability of the fast solar wind ($V_p \geq 400\ km/s$) in the $\beta_{\|p} - T_{\perp p}/T_{\|p}$ observed by PSP. The instability thresholds of different growth rate for the four instabilities (left: ion-cyclotron and parallel firehose instabilities; right: mirror mode and oblique firehose instabilities) associated with proton temperature are indicated by the lines, dotted lines, and dashed lines.
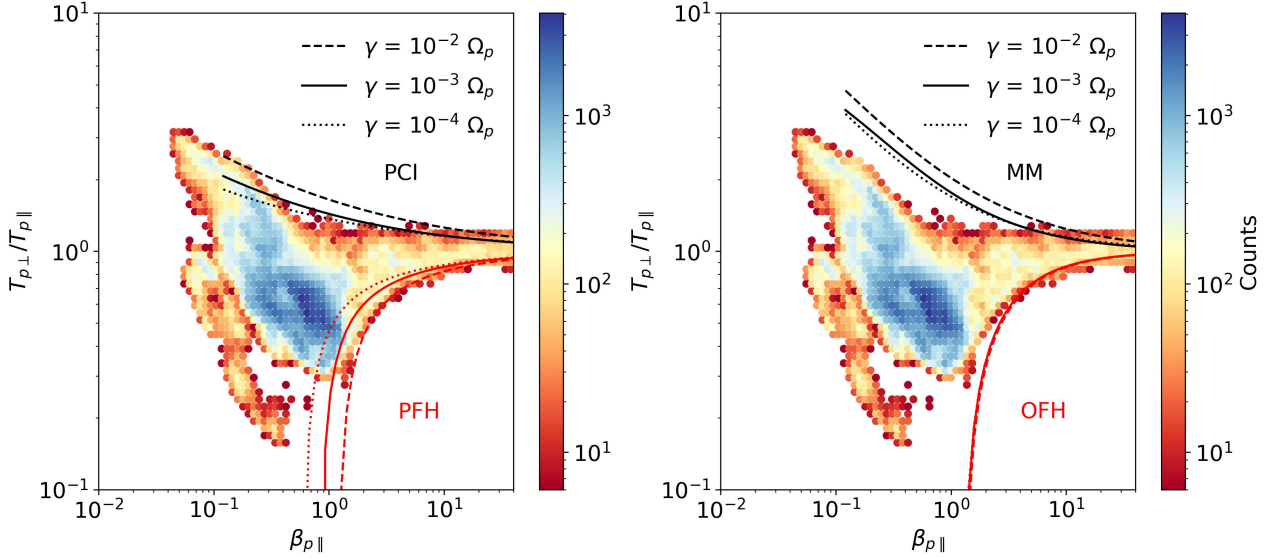

Figure 4: Probability of the fast solar wind ($V_p < 400\ km/s$) in the $\beta_{\|p} - T_{\perp p}/T_{\|p}$ observed by PSP. The instability thresholds of different growth rate for the four instabilities (left: ion-cyclotron and parallel firehose instabilities; right: mirror mode and oblique firehose instabilities) associated with proton temperature are indicated by the lines, dotted lines, and dashed lines.

portion of the distribution extends beyond the ion-cyclotron instability threshold, suggesting that ion-cyclotron instability is triggered in the fast solar wind. As for the case of slow solar wind shown in Figure 4, we can see the majority of the data is within the area marginally stable to the four instabilities. For ion-cyclotron and parallel firehose instabilities, only the marginal threshold corresponding to $\gamma = 10^{-2}\Omega_p$ mostly constraints the data in the $\beta_{p\parallel} - T_{p\perp}/T_{p\parallel}$ plane. In contrast, the data are well constrained by all of the marginal thresholds for the mirror mode and oblique firehose instabilities.

3.2 The Evolution of Non-equilibrium Features as a Function of Coulomb Collision
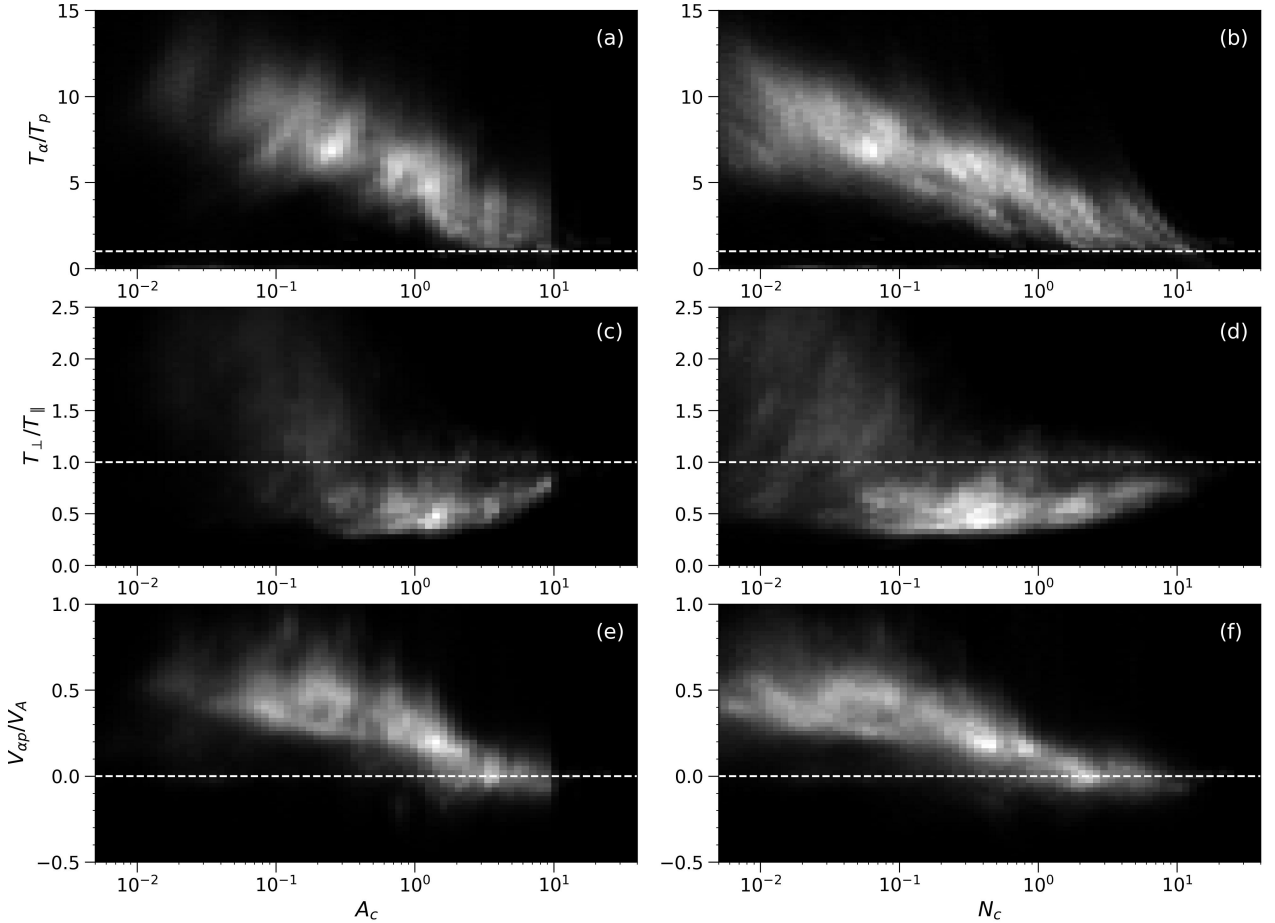

Figure 5: The distributions of the nonthermal features of the solar wind with collisional age (left) and Coulomb number (right). The nonthermal features are T_α/T_p (a, b), $T_\perp/T_\parallel$ (c, d), and $V_{\alpha p}/V_A$ (e, f), respectively.

We show in Figure 5 the distributions of the nonthermal features, including T_α/T_p, $T_\perp/T_\parallel$, and $V_{\alpha p}/V_A$, as a function of collisional age (left) and Coulomb number (right). In fact, using either Coulomb number or Collisional age in our analysis does not make a significant difference. Therefore, we use the Coulomb number (panels b, d, and f) to illustrate the impact of Coulomb collisions on nonthermal features in the solar wind. T_α/T_p is a strong function of N_c. At PSP observation regions (within 50 solar radii), when collisions are very rare, T_α/T_p can go up to about 15, which is

significantly higher than the observations at 1 AU (T_α/T_p maximum goes to $6-7$). This suggests that alphas started with relatively higher temperatures than protons at the source, and processes such as resonant interactions with waves that can preferentially heat the alphas are more pronounced at this distance. For $N_c > 1$, collisions produce thermal equilibrium, making $T_\alpha = T_p$. Measurements of $T_\perp/T_\parallel$ shows that the average value of $T_\perp/T_\parallel$ approaches 1.0 as N_c increases. Both Coulomb collisions and kinetic microinstabilities have roles in regulating proton temperature anisotropy. The evolution of the alpha-proton differential velocity has been studied in *Ran et al. (2024)* [21], here we focus on the effects of Coulomb collisions on the differential speed. As N_c increases, the differential speed approaches its equilibrium value of $V_{\alpha p} = V_A$.
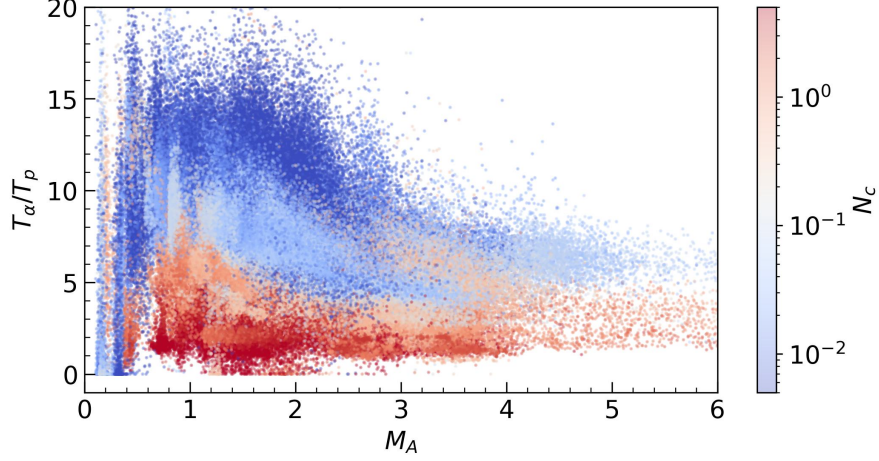

Figure 6: Measurements of T_α/T_p as a function of M_A with the colors indicating the Coulomb number.

Figure 6 shows T_α/T_p as a function of M_A with the colors indicating the Coulomb number. Note that the increase of M_A can be considered as the acceleration process of the solar wind from lower to higher altitudes. The results show that T_α/T_p increases within and around the solar corona ($M_A \leq 1$), which indicates a strong preferential heating of alphas in this region. Above the Alfvén surface, T_α/T_p decreases as M_A increases. For highly collisional plasma (red), the decrease in T_α/T_p starts at a lower M_A than for less collisional plasma (blue), and the decrease is more pronounced. This indicates that Coulomb collisions play a significant role in regulating T_α/T_p.

References

[1] Aaron Barnes. Collisionless damping of hydromagnetic waves. *The Physics of Fluids*, 9(8):1483–1495, 1966.

[2] Benjamin DG Chandran. Parametric instability, inverse cascade and the range of solar-wind turbulence. *Journal of plasma physics*, 84(1):905840106, 2018.

[3] AA Galeev and VN Oraevskii. The stability of alfvén waves. *Sov Phys Dokl*, 7, 1963.

[4] S Peter Gary. *Theory of space plasma microinstabilities*. Number 7. Cambridge university press, 1993.

[5] S Peter Gary, MD Montgomery, WC Feldman, and DW Forslund. Proton temperature anisotropy instabilities in the solar wind. *Journal of Geophysical Research*, 81(7):1241–1246, 1976.

[6] R Hernandez, S Livi, and E Marsch. On the he2+ to h+ temperature ratio in slow solar wind. *Journal of Geophysical Research: Space Physics*, 92(A7):7723–7727, 1987.

[7] R Hernandez and E Marsch. Collisional time scales for temperature and velocity exchange between drifting maxwellians. *Journal of Geophysical Research: Space Physics*, 90(A11):11062–11066, 1985.

[8] Klaus Jockers. Solar wind models based on exospheric theory. *Astronomy and Astrophysics, Vol. 6, p. 219 (1970)*, 6:219, 1970.

[9] JC Kasper, AJ Lazarus, and SP Gary. Hot solar-wind helium: Direct evidence for local heating by alfvén-cyclotron dissipation. *Physical review letters*, 101(26):261103, 2008.

[10] Justin C Kasper and Kristopher G Klein. Strong preferential ion heating is limited to within the solar alfvén surface. *The Astrophysical Journal*, 877(2):L35, 2019.

[11] Justin Christophe Kasper, Kristopher Gregory Klein, Tristan Weber, Milan Maksimovic, Arnaud Zaslavsky, Stuart D Bale, Ben A Maruca, Michael L Stevens, and Anthony W Case. A zone of preferential ion heating extends tens of solar radii from the sun. *The Astrophysical Journal*, 849(2):126, 2017.

[12] J Lemaire and M Scherer. Kinetic models of the solar wind. *Journal of Geophysical Research*, 76(31):7479–7490, 1971.

[13] E. Marsch and H. Goldstein. The effects of Coulomb collisions on solar wind ion velocity distributions. *Journal of Geophysical Research: Space Physics*, 88(A12):9933–9940, 1983. _eprint: https://onlinelibrary.wiley.com/doi/pdf/10.1029/JA088iA12p09933.

[14] Eckart Marsch. Kinetic Physics of the Solar Corona and Solar Wind. *Living Reviews in Solar Physics*, 3(1):1, July 2006.

[15] BA Maruca, JC Kasper, and SD Bale. What are the relative roles of heating and cooling in generating solar wind temperature anisotropies? *Physical Review Letters*, 107(20):201101, 2011.

[16] Bennett A Maruca, Stuart D Bale, Luca Sorriso-Valvo, Justin C Kasper, and Michael L Stevens. Collisional thermalization of hydrogen and helium in solar-wind plasma. *Physical review letters*, 111(24):241101, 2013.

[17] Bennett Andrew Maruca. *Instability-driven limits on ion temperature anisotropy in the solar wind: observations and linear Vlasov theory*. PhD thesis, Harvard University, 2012.

[18] Lorenzo Matteini, Simone Landi, Petr Hellinger, and Marco Velli. Parallel proton fire hose instability in the expanding solar wind: Hybrid simulations. *Journal of Geophysical Research: Space Physics*, 111(A10), 2006.

[19] P Mostafavi, RC Allen, VK Jagarlamudi, S Bourouaine, ST Badman, GC Ho, NE Raouafi, ME Hill, JL Verniero, DE Larson, et al. Parker solar probe observations of collisional effects on thermalizing the young solar wind. *Astronomy & Astrophysics*, 682:A152, 2024.

[20] V Pierrard, H Lamy, and J Lemaire. Exospheric distributions of minor ions in the solar wind. *Journal of Geophysical Research: Space Physics*, 109(A2), 2004.

[21] Hao Ran, Ying D Liu, Chong Chen, and Parisa Mostafavi. The alpha-proton differential flow in the alfvénic young solar wind: From sub-alfvénic to super-alfvénic. *The Astrophysical Journal*, 963(2):82, 2024.

[22] RZ Sagdeev and AA Galeev. Nonlinear plasma theory. *Benjamin, New York*, 1969.

[23] RW Schunk. Transport equations for aeronomy. *Planetary and Space Science*, 23(3):437–485, 1975.

[24] Lyman Spitzer and Charles J Cook. Physics of fully ionized gases: No. 3 of interscience tracts on physics and astronomy. *Physics Today*, 10(1):40–42, 1957.

[25] Daniel Verscharen, Kristopher G. Klein, and Bennett A. Maruca. The multi-scale nature of the solar wind. *Living Reviews in Solar Physics*, 16(1):5, December 2019.

[26] Lynn B Wilson III, Michael L Stevens, Justin C Kasper, Kristopher G Klein, Bennett A Maruca, Stuart D Bale, Trevor A Bowen, Marc P Pulupa, and Chadi S Salem. The statistical properties of solar wind temperature parameters near 1 au. *The Astrophysical Journal Supplement Series*, 236(2):41, 2018.

[27] L. D. Woodham, T. S. Horbury, L. Matteini, T. Woolley, R. Laker, S. D. Bale, G. Nicolaou, J. E. Stawarz, D. Stansby, H. Hietala, D. E. Larson, R. Livi, J. L. Verniero, M. McManus, J. C. Kasper, K. E. Korreck, N. Raouafi, M. Moncuquet, and M. P. Pulupa. Enhanced proton parallel temperature inside patches of switchbacks in the inner heliosphere. *Astronomy & Astrophysics*, 650:L1, June 2021.